*remote sensing*

MDPI

*Article*

# Taking Advantage of the ESA G-POD Service to Study Ground Deformation Processes in High Mountain Areas: A Valle d'Aosta Case Study, Northern Italy

**Martina Cignetti [1,*], Andrea Manconi [2], Michele Manunta [3], Daniele Giordan [1], Claudio De Luca [3], Paolo Allasia [1] and Francesca Ardizzone [4]**

1 National Research Council of Italy, Research Institute for Geo-Hydrological Protection (CNR-IRPI), Strada delle Cacce 73, 10135 Torino, Italy; daniele.giordan@irpi.cnr.it (D.G.); paolo.allasia@irpi.cnr.it (P.A.)
2 Departement of Earth Sciences, Engineering Geology, ETH Zürich, Sonneggstrasse 5, NO G65, CH-8092 Zürich, Switzerland; andrea.manconi@erdw.ethz.ch
3 National Research Council of Italy, Istituto per il Rilevamento Elettromagnetico dell'Ambiente (CNR-IREA), via Diocleziano 328, 80124 Napoli, Italy; manunta.m@irea.cnr.it (M.M.); deluca.c@irea.cnr.it (C.D.L.)
4 National Research Council of Italy, Research Institute for Geo-Hydrological Protection (CNR-IRPI), Via della Madonna Alta 126, 06128 Perugia, Italy; francesca.ardizzone@irpi.cnr.it
* Correspondence: martina.cignetti@irpi.cnr.it; Tel.: +39-011-397-7831

Academic Editors: Roberto Tomas, Zhenhong Li and Prasad S. Thenkabail
Received: 15 July 2016; Accepted: 11 October 2016; Published: 20 October 2016

**Abstract:** This paper presents a methodology taking advantage of the GPOD-SBAS service to study the surface deformation information over high mountain regions. Indeed, the application of the advanced DInSAR over the arduous regions represents a demanding task. We implemented an iterative selection procedure of the most suitable SAR images, aimed to preserve the largest number of SAR scenes, and the fine-tuning of several advanced configuration parameters. This method is aimed at minimizing the temporal decorrelation effects, principally due to snow cover, and maximizing the number of coherent targets and their spatial distribution. The methodology is applied to the Valle d'Aosta (VDA) region, Northern Italy, an alpine area characterized by high altitudes, complex morphology, and susceptibility to different mass wasting phenomena. The approach using GPOD-SBAS allows for the obtainment of mean deformation velocity maps and displacement time series relative to the time period from 1992 to 2000, relative to ESR-1/2, and from 2002 to 2010 for ASAR-Envisat. Our results demonstrate how the DInSAR application can obtain reliable information of ground displacement over time in these regions, and may represent a suitable instrument for natural hazards assessment.

**Keywords:** high mountain regions; ground surface deformation; DInSAR; GPOD-SBAS

## 1. Introduction

Glaciers and paraglacial processes, as landslides and rock glaciers, play an important role in the short- and long-term landscape evolution of high mountain regions [1–3]. Changes in climatic conditions, as well as human activity, can have a severe influence on such geomorphological processes, and increase the frequency and intensity of catastrophic mass wasting events [4,5]. In alpine regions, glaciation has been recognized as one of the most important agents influencing the regional geomorphology [6,7]. Indeed, several geological and geomorphological studies have outlined the relation between large slope instabilities and deep-seated gravitational slope deformation located in glacial valleys, likely due to the debuttressing caused by glacier retreat [8–11].

In this scenario, monitoring surface deformation in high mountain regions can help to better interpret the kinematic behavior of mass wasting processes, and to infer potential influences of

meteo-climate variables on their evolution [12–14]. This information is crucial to increase our capability to assess landslide hazards, and to manage the associated risks [15–18]. In recent decades, surface deformation in mountain environments has been measured by means of diverse monitoring approaches, ranging from classical in situ instruments [19–24] to more advanced remote sensing methods [25–28]. In situ instruments are typically installed to obtain a time series with high temporal resolution, which allows for a better analysis of local phenomena over time, while remote sensing techniques are more suitable for the evaluation of deformation trends at regional scales. Among different techniques, space-borne differential synthetic aperture radar (SAR) interferometry (DInSAR) has gained an important role in measuring ground displacements over the last few years [29]. DInSAR is a consolidated method used to provide data with extensive spatial coverage and to investigate different types of phenomena simultaneously, including those hindered by limited or difficult access. For example, DInSAR was successfully applied to detect and monitor slow movements of mountain slopes in the order of few centimeters/year in the Austrian and Swiss Alps, and the Pyrenees, confirming its operational potential in high mountain areas [30–32].

Advanced DInSAR methods have been developed to derive ground velocity maps and displacement time series [33–35]. The small baseline subset (SBAS) technique [34], which combines sets of interferograms with small orbital separation (baseline) and short revisiting time to reduce the temporal decorrelation and maximize the number of coherent SAR targets, has proven to be suitable in different deformation scenarios [36–39]. Accuracies are in the order of 1 mm/year for mean surface velocities and 5 mm for displacement measurements [40].

Nowadays, the increasing availability of multi-temporal satellite acquisitions allows for the generation of time series of ground deformation spanning periods as long as 20 years. This information is particularly suitable for studying the long-term behavior of landslides, rock glaciers, and glaciers. However, the analysis of surface deformation via DInSAR is challenging for several reasons, including (i) the high topographic gradients associated with the complex orography; (ii) abundant vegetation affecting the temporal correlation of the SAR signal; and (iii) unsuitable valley flank orientations relative to the SAR view angle [41–44]. Moreover, DInSAR ground deformation monitoring for systematic analyses is complicated due to the intrinsic limitations of the technique (i.e., coherence loss due to large revisit time, phase decorrelation due to large or rapid displacement, and line-of-site (LOS) measurements only) [33,45–47]. Additional issues are caused by the atmospheric phase screen (APS), which is amplified by high topographic gradient in high mountain regions. The APS, caused by the atmospheric pressure, temperature, and water vapor variations between two SAR acquisitions, may cause artifacts on the surface deformation results [48]. Moreover, SAR images acquired in winter periods are highly affected by snow cover, which causes temporal coherence loss [47,49,50].

All these factors have to be carefully taken into account for SAR data processing to thoughtfully interpret the ground deformation in high mountain regions. In several cases, however, the complexity of SAR data processing, as well as the large number of attempts to be performed before obtaining reliable results, hinders the achievement of surface deformation results. Currently, the application and the treatment of SAR data in high mountain regions requires specific background knowledge of the user and demand the application of complex processing algorithms and software. Moreover, the increasing amount of SAR data available from different satellites missions leads to rising needs of storage and computing resources. Recently, a relevant service was released within the ESA GRID-based operational environment [51], i.e., the unsupervised implementation of the Parallel-SBAS (P-SBAS) algorithm [52]. GPOD is coupled with high-performance and sizeable computing resources managed by GRID technologies, and it provides flexibility for building an application virtual environment with quick accessibility to data, computing resources, and results. The users access various services useful in the EO applications through a web interface, which guides the users from the creation of a new task until the results publication, passing through the data selection and the job monitoring. The P-SBAS algorithm has been implemented to exploit the GPOD resources, and to process the SAR data archived by ESA to perform the full SBAS-DInSAR processing chain in an unsupervised fashion from the

Level 0 (raw) SAR data to the generation of surface velocity maps and displacement time series [53]. Since the average processing time is smaller than 24 h, several processing attempts can be performed in a reasonable time-span to optimize the final results on a specific target area. The main advantage of this service, hereafter referred to as GPOD-SBAS, is that users with different backgrounds, more interested in the analysis of the surface deformation due to different natural and/or anthropic processes than in the details of the SAR data processing, can apply a reliable and validated state of the art algorithm without downloading large amounts of input data, nor owning costly processing hardware or learning specific software [53].

In this study, we define best practices to obtain surface displacement time series in high mountain regions by using the GPOD-SBAS service. Our work derives from a specific need: even though the unsupervised GPOD-SBAS service provides a great advance and allows a larger number of users to carry out advanced DInSAR analyses, obtaining reliable results in mountain areas is not a trivial task. The proposed methodology is applied to the Valle d'Aosta (VDA) region, Northern Italy, an alpine area characterized by high altitudes, complex morphology, and susceptibility to different mass wasting phenomena (e.g., landslides, rock glaciers, and glaciers), in some cases threatening urban areas and human activities, and it can be easily borrowed in similar areas.

The paper is organized as follows. We first introduce the area of study by highlighting the geomorphological, environmental, and climatic characteristics. Then, we describe the method applied to analyze, through the use of the GPOD-SBAS service, the data acquired by ERS-1/2 and ASAR-Envisat during the 1992–2000 and 2002–2010 periods, respectively, in ascending orbit for ERS-1/2, and in ascending and descending orbit for ASAR-Envisat. Finally, we present the results, discuss our findings, and propose a number of suggestions and best practices to be considered to retrieve effective and reliable information while approaching the analysis of SAR data in high mountain areas.

## 2. The Valle d'Aosta Region, Northern Italy

The Valle d'Aosta region (3200 km$^2$) is located in the Northwestern Italian Alps (Figure 1). More than 50% of the Valle d'Aosta (VDA) territory has an elevation above 2000 m a.s.l., though topographic relief is highly variable, ranging from 300 m a.s.l. to peaks higher than 4000 m a.s.l. (e.g., Mt. Bianco, 4810 m a.s.l.; Mt. Rosa, 4635 m a.s.l.; Cervino, 4478 m a.s.l.: Gran Paradiso, 4061 m a.s.l.).

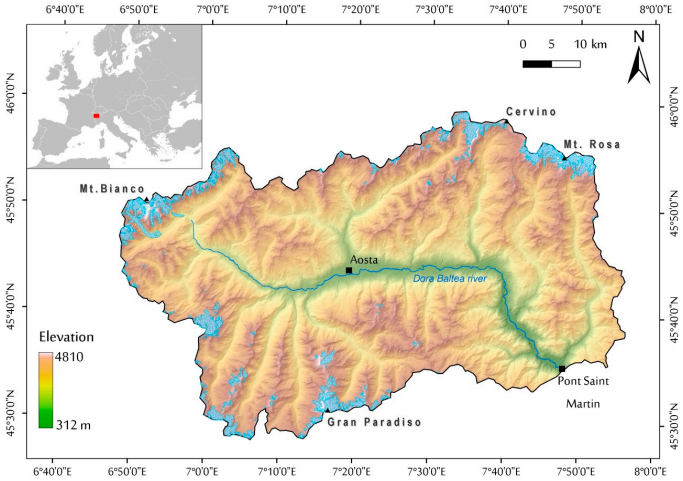


**Figure 1.** Relief terrain of the study area (the Valle d'Aosta (VDA) region, Northwestern Italy). The map shows the high and complex morphology of this mountainous area; the **light blue** polygons correspond to the present glaciers of the region, modified from the Glacier map of Fondazione Montagna Sicura [54].

From a geological point of view, the VDA region is part of the alpine chain [55–59], passing through the principal Europe-vergent Austroalpine-Penninic structural domain of the Western Alps. The Valley

presents a complete section of the orogenic prism including (i) the Austroalpine domain; (ii) the ophiolitic Piedmont zone; and (iii) the Pennidic domain. These tectonic-metamorphic units composed of a complex pile of nappes, which present a post-collisional tectonic activity and a neo-tectonic dislocation system activation (e.g., semi-graben Aosta-Ranzola fault) [57]. The morphological traits of the VDA are characterized by the main valley trending east–west (Dora Baltea Valley). This is a wide (3400 $km^2$) glacial valley with several tributary valleys (trending north–south), which ends around the Pont Saint Martin municipality, at the Ivrea moraine amphitheater, the main evidence of Quaternary glaciations [60].

As typical in alpine valleys, VDA has a prevalence of highly vegetated areas, while human settlement distribution is located at the valley bottom. The land cover is prevalently represented by forest, natural grassland, and rock outcrops with little or no vegetation. In addition, the massifs dominating the VDA landscape act as morphological boundaries and deeply influence the local climatic conditions. Indeed, the high peaks limit the access of air masses from the Mediterranean Sea or the Atlantic Ocean, causing a clear difference in the rain and snow precipitation regimes [61]. The regional climate, in mountainous and marginal sector, is characterized by wide range of temperatures and rainfall/snowfall (min, max and average values of 1000–1100 mm/year, while, in correspondence of the principal valley bottom, by a temperate climate, characterized by relatively lower rainfall (lower than 600 mm/year) [62].

### *2.1. Mass Movement in the Valle d'Aosta Region*

The slopes of VDA are characterized by high density of mass movements, which can be synthetically grouped in glaciers, rock glaciers, and landslides. These phenomena are mainly related to the long- and short-term evolution of glacial, periglacial, and paraglacial processes [63,64]. Glaciers nowadays occupy as much as 5% of the regional territory, which represent one-third of the Italian glaciers [65]. The rate of ground deformation vary significantly passing from glacier flows, which is characterized by rates of tens to hundreds of meters per year, to permafrost creep, in order of cm to m per year [63,66,67]. The alpine permafrost has a very variable and fragmented distribution, showing creep deformation depending on permafrost temperature [68]. Rock glaciers (RGs), i.e., periglacial landforms common in high alpine environments, occupy about 2% of the VDA territory [69,70]. RGs are defined as lobate to tongue-shaped structure of frozen rock debris, with steep front and side slopes, interstitial ice cement, ice lenses, a core of massive ice, or a combination thereof. These ice-rocky structures may creep depending on the mountain permafrost condition. Due to the ice content, the RGs are classified as active, inactive, or relict [70–72]. Active RGs have higher ice content and move downslope with velocities ranging from several cm/year to several m/year [73]. Inactive RGs contain some ice, but do not move. Finally, relict RGs present a front slope less steep gradient and are frequently covered by vegetation, do not contain ice, and do not move. In VDA, 937 rock glaciers were identified, and most of them (56%) were classified as relict [74–76]. The intact RGs are located at a higher altitude, presenting a lower limit variable from 2126 m and 3150 m a.s.l., and a prevalently northeast-to-northwest exposure. The relict RGs are located not below 1600 m a.s.l. altitude, and reach on average at the upper limit of 2700 m a.s.l., presenting variable exposure.

Another important gravitational process that affects 18% of the VDA territory [77,78] are landslides. These phenomena vary in size and typology, from shallow landslides (soil slips, planar, and rotational sliding) to large slope instabilities. In the VDA region, deep-seated gravitational slope deformations (DsGSDs) affect at least 13.5% of the regional territory [77], for a total of 280 phenomena inventoried. These large slope instabilities are widespread phenomena in mountain areas of the entire European Alps [11,79] and represent a large mass movement of an entire high-relief flank valley [80]. Their evolution is controlled by the interaction of different factors: lithology, geology, climate weathering, seismicity, and deglaciation [11]. In most cases, DsGSDs are located in initially glacial valleys and related to Lateglacial trigger [80]; for these phenomena, the major cause of instability is ascribed to glacial debuttressing. These phenomena generally present very slow–slow deformation rates, variable from a few millimeters per year to a maximum of a few centimeters per year in uncommon cases [81].

### 2.2. Challenges for Retrieving Surface Deformation with DInSAR of VDA

The geomorphological and meteo-climatic characteristics make VDA a challenging environment for the analysis of surface deformation with DInSAR, including (i) a high topography gradient, (ii) complex orography, (iii) a predominance of forest or abundant vegetated areas, and (iv) unsuitable valley flank orientations, specifically due to the alternatively west- and east-facing orientation of the tributary valleys.

By assuming ERS-1/2 and ASAR-Envisat acquisitions, we aim at understanding the theoretical distribution of scatters in the VDA region. This analysis has been carried out by computing the R-Index [82], which considers slope and aspect angles of the ground surface, as well as the satellite's incident acquisition geometry (incident angle, i.e., 23°, and an azimuth angle of the satellite orbit from north (clockwise), i.e., 345° in ascending orbit and 195° in descending orbit, respectively). The resulting map reveals, for the north–south oriented valleys, layover (thus less exploitable scatters) on the west-facing slope in ascending orbit (Figure 2a) and layover on the east-facing slope in descending orbit (Figure 2b). On the other end, east–west oriented valleys experience layover or foreshortening on the north-facing slopes in ascending orbit and the south-facing slope in descending orbit.

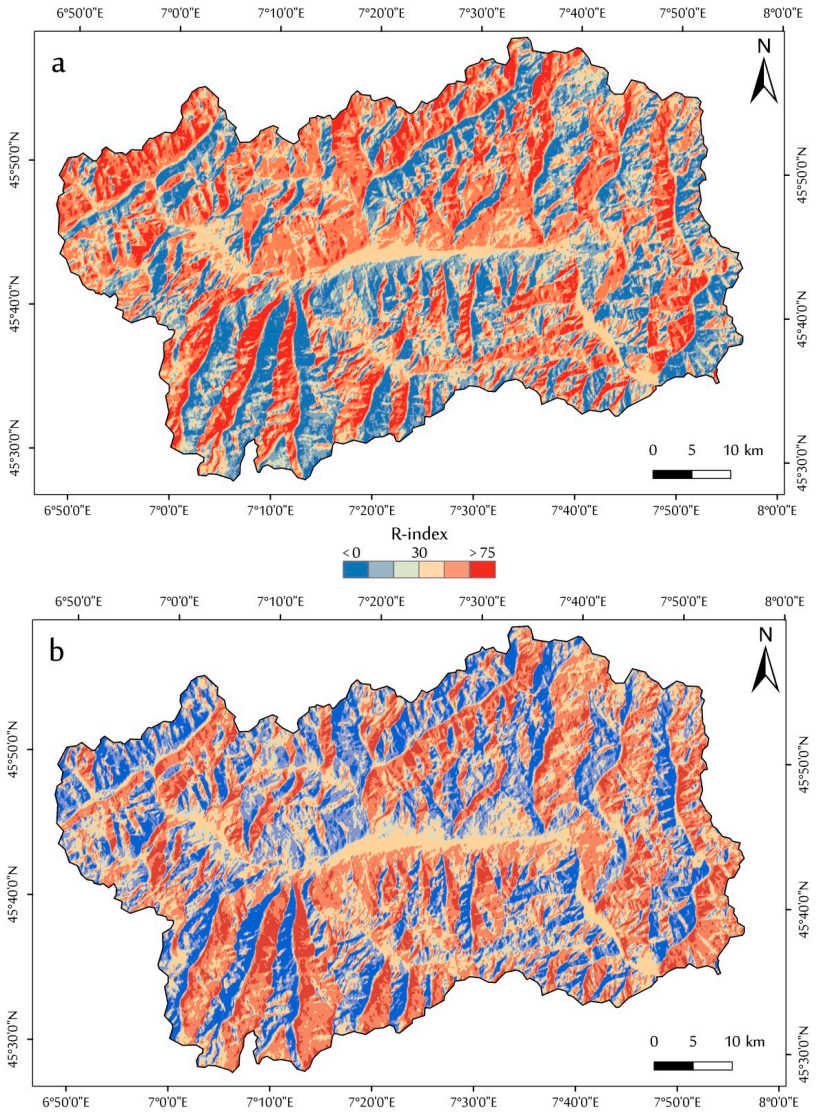


**Figure 2.** R-Index map (**a**) of the ascending orbit and (**b**) of the descending orbit for the VDA region. Layover/foreshortening cases are present for values lower than zero (**blue** portion).

Furthermore, land use is also an important factor that has effects on the SAR result distribution (Figure 3). The prevalence of natural and high-vegetated areas for the entire VDA regional territory generates temporal decorrelation effects [47]. In addition, temporal coherence loss may occur due to the meteo-climatic conditions of the investigated area, characterized by a prevalent snow cover during the winter season.

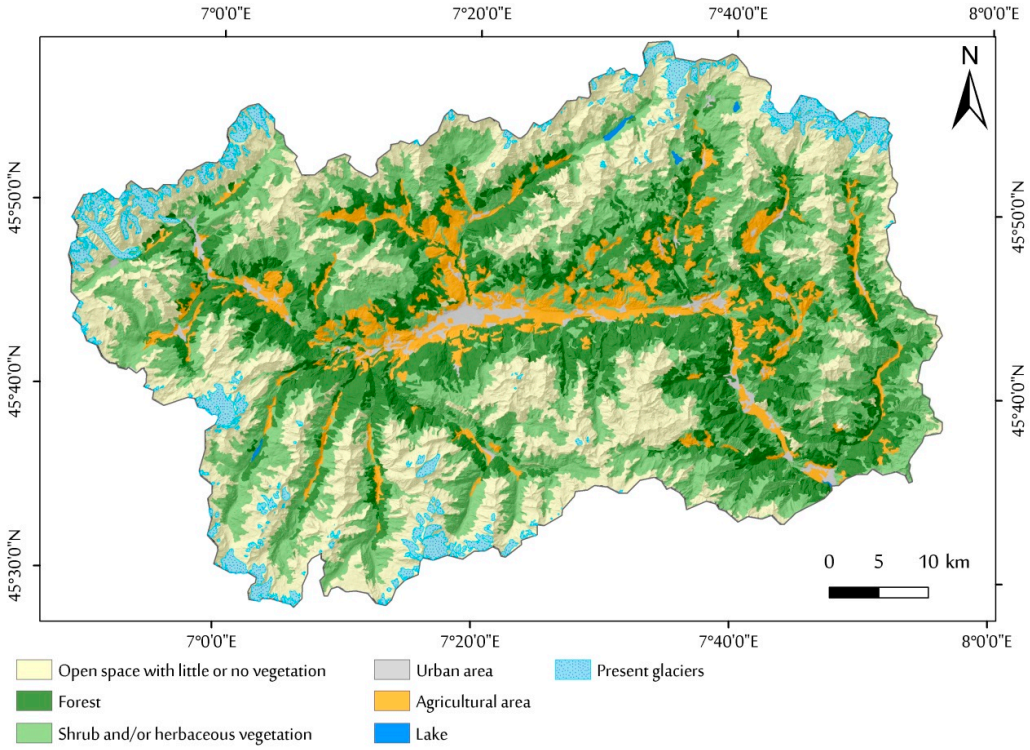


**Figure 3.** Land cover map of the VDA region (redraw from CORINE 2006).

## 3. Methods

By taking into account the challenges outlined above, here we present a methodology to exploit the capabilities and potentialities supplied by the GPOD-SBAS service to retrieve the surface deformation information over high mountains. The VDA region is a representative area of investigation where we apply GPOD-SBAS processing.

We consider SAR images collected by ERS-1/2, in ascending orbit, and ASAR Envisat missions from ascending and descending orbits (see Table 1). The tracks cover most of the VDA regional territory, excluding only about 10% of the entire region localized in the eastern portion (see Figure 4). The reference point is selected corresponding to an area assumed stable, on the basis of geological and geomorphological background analysis, during the investigation period, and where DInSAR coherence values are expected to be high (i.e., within the Aosta municipality, see Figure 4).

**Table 1.** Summary of the ERS-1/2 and ASAR Envisat images considered for the VDA study area.

| Satellite | Observation Period | Track | Frame | Orbit Acquisition | Number of Images |
|---|---|---|---|---|---|
| ERS-1/2 | April 1995–May 2000 | 301 | 909 | Ascending | 32 |
| ENVISAT | June 2004–October 2010 | 301 | 909 | Ascending | 50 |
| ENVISAT | September 2004–October 2010 | 294 | 2673 | Descending | 46 |

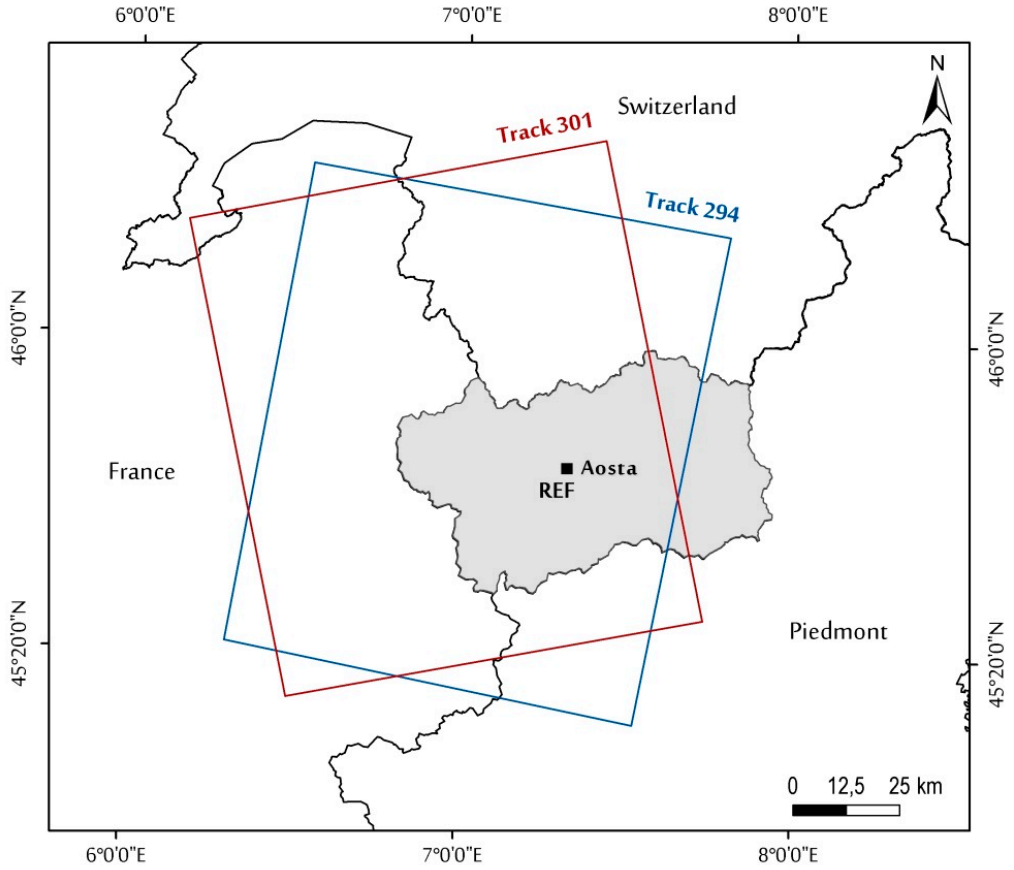


**Figure 4.** Map of the VDA region study area (in **light grey**). The **red** box represents the extent of ERS-1/2 and ASAR Envisat track in ascending orbit, while the **blue** box represents the track in descending orbit. The reference point (REF) is located in the Aosta municipality.

Though the SBAS approach can be jointly applied to ERS-1/2 and ASAR Envisat datasets to retrieve a continuous time series covering almost 20 years [83], at the moment of the processing, the implementation available in GPOD allows us to process the datasets only separately. To retrieve reliable results and to maximize the spatial coverage of the achieved coherent points, we perform an iterative procedure in order to choose the most suitable SAR dataset, to minimize the temporal decorrelation effects mainly related to the presence of snow cover in the areas of interest, and to preserve the processing of the largest number of SAR scenes. We perform four tasks (named from T1 to T4) for each orbit, summarized in Table 2. It is worth noting that such an analysis phase, addressed to select the most suitable dataset, plays a key role when analyzing mountain areas. Indeed, the presence of several decorrelation sources, i.e., vegetation and snow cover, requires proper identification of the SAR acquisitions less affected by noise through an iterative mechanism. This analysis can be easily and efficiently carried out within the GPOD environment thanks to its capability to perform SBAS analyses in a reasonably short time (about 24 h). As a final remark, the following analysis is based on the two available Envisat datasets because they have a good number of SAR acquisitions (more than 50 acquisitions) uniformly distributed during the observed time period, and permit a better investigation of the impact of winter acquisition on the final results. As regards ERS-1/2 dataset, due to the limited number of available SAR acquisitions, it is directly processed by selecting the images and the processing parameters on the basis of the Envisat analyses. Finally, we advise that GPOD-SBAS operates with the three-arcsec DEM free available from the SRTM archive.

**Table 2.** Summary of the features of the attempts processed by the GPOD-SBAS service for the ASAR Envisat database in the VDA study area, also reporting the different values of the GPOD-SBAS processing parameters.

| Attempt | Satellite | Orbit | Images | Results (Number of Targets) | Increment from T1 (%) | Ground Pixel Size (m) | Coherence Threshold |
|---|---|---|---|---|---|---|---|
| T1 | ENV | ASC<br>DESC | 50/50<br>46/46 | 4598<br>2143 | | 80 | 0.7 |
| T2 | ENV | ASC<br>DESC | 38/50<br>38/46 | 13343<br>5987 | 193%<br>179% | 80 | 0.7 |
| T3 | ENV | ASC<br>DESC | 37/50<br>37/46 | 19011<br>9748 | 313%<br>355% | 80 | 0.7 |
| T4 | ENV | ASC<br>DESC | 37/50<br>37/46 | 33086<br>20317 | 620%<br>848% | 40 | 0.8 |

In T1, we processed all the available images for each Envisat dataset by keeping the default parameters of the GPOD-SBAS unmodified; this task is very important because it allows us to produce a large number of interferograms involving all the available SAR scenes and to retrieve a complete overview of the whole SAR dataset. Moreover, the results achieved represent a backbone analysis carried out with the maximum number of available acquisitions; thus, they provide a deformation time series with the highest temporal sampling. However, the spatial distribution of resulting coherent targets is limited.

In order to increase our capacity for image surface deformation phenomena, in T2 we reprocessed only the images acquired from April to November without changing any other input or parameter, assuming that the snow season in VDA corresponds to the December–March period [84]. The approach followed in T2 can be particularly critical because it introduces very long temporal gaps in the SAR dataset during the winter periods and can strongly reduce the number of available acquisitions. Moreover, it does not guarantee the removal of all acquisitions affected by snow cover because the climatic conditions in mountain areas can significantly change year-by-year and zone-by-zone. However, the second analysis significantly improved the number of targets with respect to the first one: if we consider, for example, the Envisat ascending data, we registered an increase in the number of targets of 193% (Table 2).

As stated above, snow seasons in VDA mainly range from December to March; however, there are exceptions. For example, the 2008–2009 winter registered extraordinary snow season from November to May [84]. According to this experience, in T3 we improved the SAR image selection method throughout the analysis of meteorological records coeval to SAR observation. Considering several weather stations of the regional meteorological network, a day-by-day analysis in correspondence to the satellite acquisition epochs is carried out. All the considered weather stations [85] are located above 2000 m a.s.l. to guarantee the significance of the meteo-climatic measurements for high mountain environments. This analysis is performed in two phases: (i) snow coverage identification and (ii) interferogram evaluation. In particular, we examined the daily rainfall (in mm) and the snow depth (in cm) parameters. The images characterized by abundant rain or snow precipitation were discarded from further analyses. Successively, an interferogram analysis was performed to identify SAR acquisition strongly affected by snow cover. During this analysis, arbitrary thresholds were considered. We observed that over 50 cm in snow depth could generate noisy interferograms. Regarding rainfall, only a single image was discarded from the analysis (28 May 2007), associated with a rainfall event of more than 30 mm/day, which has also generated, in this case, noisy interferograms. According to the analysis of the meteo-climatic parameters, we discarded only the images associated with the most critical values of daily rainfall and snow depth to ensure the SBAS processed the largest number of acquisitions. Using this fine-tuning, in T3 we still improved the number of targets: considering the Envisat ascending orbit again as a reference, the increment of coherent points with respect to the first analysis is of 313% (Table 2); with respect to T2, an increase in the number of targets to 5668 was revealed.

It is worth noting that, for the reliability of the SBAS-DInSAR analysis, it is very important to keep in the processed dataset a number of SAR acquisitions as large as possible to preserve a good temporal sampling and to limit as much as possible the presence of temporal gaps [86]. Accordingly, we only removed the SAR acquisitions affected by a widespread snow cover that clear impacts on the spatial coherence of the interferograms. To this aim, it was crucial to crosscheck the meteo-climatic conditions that provide local information and with the quality of the interferograms that supply large-scale information.

Finally, in T4, we performed a final tuning of the processing parameters [53], such as the ground pixel dimension (from 80 m to 40 m) and the coherence value of the analyzed pixels (from 0.7 to 0.8), while the default values of the maximum perpendicular (400 m) and temporal baseline (1500 days) were maintained. The increment of the number of targets (Envisat ascending orbit) for this last processing corresponds to about 620%.

Similar or even larger increments were observed for the Envisat descending analysis (Table 2). The significant increment of coherent targets due to the fine-tuning of the processing parameters in T4 is worth noting. This can be mainly explained by the coherence value used in this task. This parameter allows users to define the selection of the pixels to be considered in the SBAS analysis by changing the spatial network of the pixels to be unwrapped [87]. The default value in the GPOD-SBAS service is 0.7, and it is suitable for a very large number of test sites. However, in some particular sites, the presence of a very large number of target with poor coherence can hinder the phase unwrapping (PhU) operation [87] within the GPOD-SBAS service processing chain. In these cases, the PhU results can be significantly improved if only the targets with very high coherence are selected. This generally happens in mountain areas, where the pixels are characterized by lower coherence values and, moreover, have a sparse distribution over the scene, thus making PhU step a challenging operation.

## 4. Results

By exploiting the GPOD-SBAS, we obtained mean deformation velocity maps and displacement time series for the VDA regional territory, covering a time interval of more than 4 years (ERS-1/2) and of more than 6 years (ASAR-Envisat), respectively (see also Figure S1). Table 2 summarizes the testing activity done to perform the iterative procedure implemented for the high mountain region, operating on the Envisat dataset, and later directly applied to the ERS-1/2 dataset. All of the processed tasks were successfully completed by the unsupervised GPOD-SBAS service in less than 24 h. Depending on the SAR images considered, and on the processing parameters applied, we obtained a different amount of coherent targets (see Table 2). In Figure 5, we show the distribution of coherent targets subdivided according to slope class, obtained by the slope calculation from a DTM with 10 m square grid spacing for each processed task of the Envisat datasets. We note that, for all the datasets, we have a general increase in the number of coherent targets for all slope classes. In the first task T1, the prevalent distribution corresponds to the lowest degree slope (0°–20°), coincident to the most urbanized areas, corresponding to the most coherent sectors. On the contrary, on the high to very high classes (40°–60° and >60°), we note a general lack of target distribution. However, the number of targets obtained in T4 is as large as one order of magnitude with respect to T1.

In Figures 6 and 7, we present the best results obtained for both Envisat (ascending and descending orbits) and ERS (ascending orbit) datasets (see also Figure S1). Coherent targets are mainly located at the main valley bottom, where urbanized areas (e.g., streets, railway, main towns, hamlets, and isolated building) are located. Within the observed period, LOS velocities in these areas are rather small, ranging from about $\pm$0.2 cm/year and comparable between Envisat and ERS processes, confirming an overall ground stability. Relative to the ERS-1/2 dataset, directly processed on the basis of the results achieved with the Envisat analysis, a significantly lower data coverage respect to the Envisat resulted, presenting a total amount of targets of 8574. As expected from the SAR visibility analysis performed (see Figure 2), coherent target distribution is mainly on east-facing slopes, in ascending orbit, and on west-facing slopes, in descending orbit. Moreover, in the valleys, targets are mainly localized in hamlets and villages, as well as in areas of little or no vegetation (e.g., talus, moraine, and bare rock).

From the comparison between the GPOD-SBAS process results and the known distribution of the VDA gravitational process considered in this work, we notice that, in correspondence to glaciated sectors, a decorrelation effect due to their large displacement, and a consequently total absence of targets, was revealed.

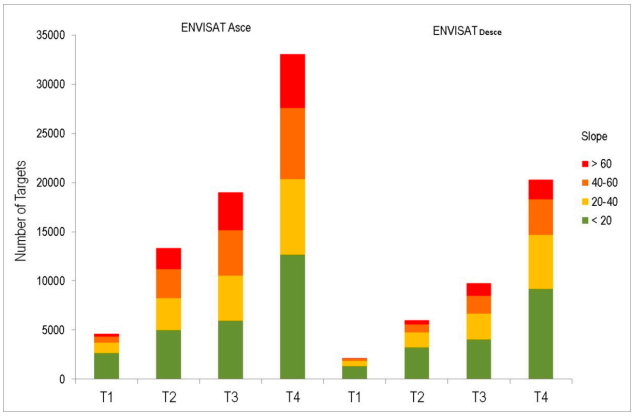


**Figure 5.** Graph of the number of targets of each dataset available for the Envisat satellite for each task processed. The targets are subdivided and classified with respect four slope classes, based on the slope calculation of the VDA region.

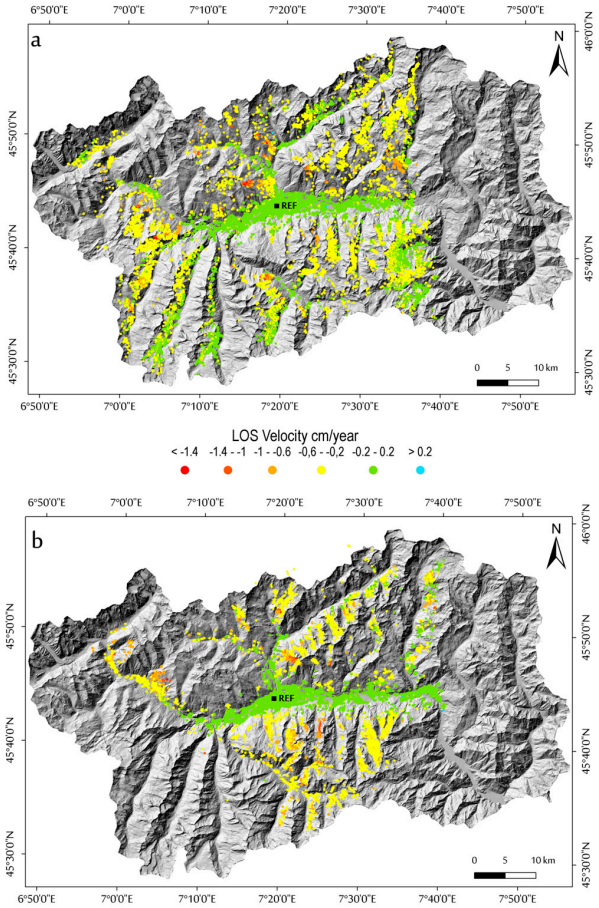


**Figure 6.** Surface velocities measured along the satellite LOS for the Envisat dataset: (**a**) in ascending orbit for the time period from June 2004 to October 2010 and (**b**) in descending orbit for the time period from September 2004 to October 2010. The **light blue** polygons correspond to the present glaciers.

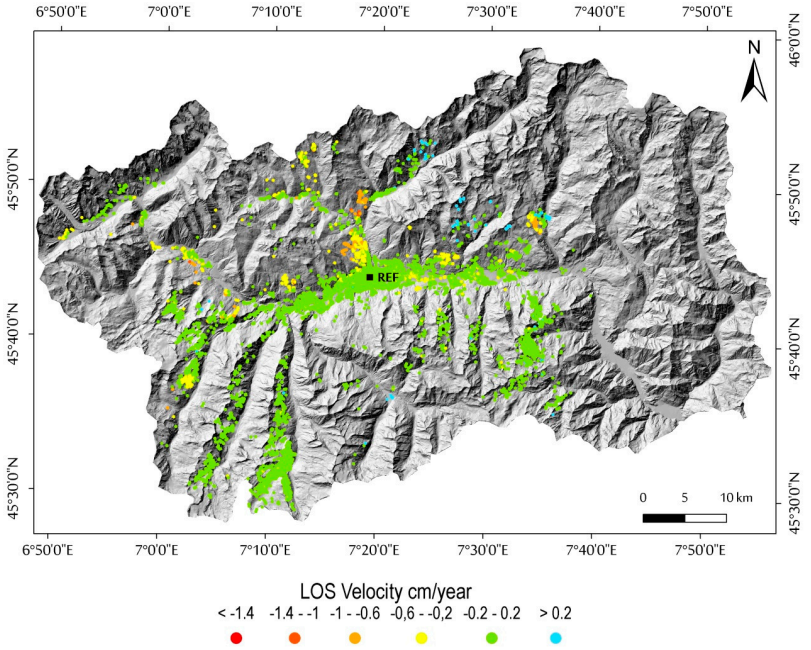


**Figure 7.** Surface velocities measured along the satellite LOS for the ERS-1/2 dataset in ascending orbit for the time period from June 1995 to May 2000. The **light blue** polygons correspond to the present glaciers.

### *4.1. Deep-Seated Gravitational Slope Deformations*

We compared the ground velocity map obtained through the GPOD-SBAS processing to the DsGSD phenomena present in the area of investigation, according to the IFFI (Italian Landslides Inventory) catalogue [88], and found a good correlation between deforming areas observed and the occurrence of DsGSD phenomena. We performed this comparison making use of Envisat results (both ascending and descending orbits), which present the best coverage of the VDA study area and a higher number of targets with respect to the ERS-1/2 results. Considering the ascending orbit, the inventoried DsGSDs included within the track considered are 179, and only 44% present targets inside, of which 25% present more than ten targets. Considering the descending orbit, 191 DsGSDs inventoried are included within the track considered; in this case, 35% of these phenomena present targets inside, of which only 19% present more than ten targets (Table 3). Moreover, the highest coherent target density for the east face-oriented DsGSD cases in ascending orbit, and for the west face-oriented DsGSD cases in descending orbit was observed.

**Table 3.** Summary of the number of deep-seated gravitational slope deformations (DsGSDs) inventoried in the IFFI project covered by targets generated by the GPOD-SBAS process.

| | DsGSD (from IFFI) | Number of DsGSD (within the Track) | Number of DsGSD Covered by Targets | Number of DsGSD with >10 Targets |
|---|---|---|---|---|
| ENVISAT Ascending | 280 | 179 | 79 | 44 |
| ENVISAT Descending | | 191 | 66 | 36 |

Two specific examples are reported and illustrated in Figures 8 and 9. The first example is the Beauregard DsGSD, located in the southwest portion of the region, while the second is the Quart DsGSD, located in the middle portion of the principal valley.

The Beauregard DsGSD is an extended phenomena, going from 1700 m a.s.l., close to the valley bottom, up to 2900 m a.s.l. in the northern sector, corresponding to its main scarp. In [89], a non-homogeneous deformation pattern of this phenomenon is described, with the upper part

presenting the highest displacement rates, and a slow and constant deformation along the basal portion of the phenomenon.

Exploiting our results (Figure 8a), we noted a good density of the target distribution, higher than that in other DsGSDs. The target distribution mainly covers the upper-northern and the central sector, while no targets were revealed in the southern part and in general at the DsGSD toe, where only a small basal portion of the landslide close to the dam structure is covered. The distribution of the targets is influenced by the distribution of bedrock outcrops: in the area covered by grassland or woods, the number of targets is very poor.

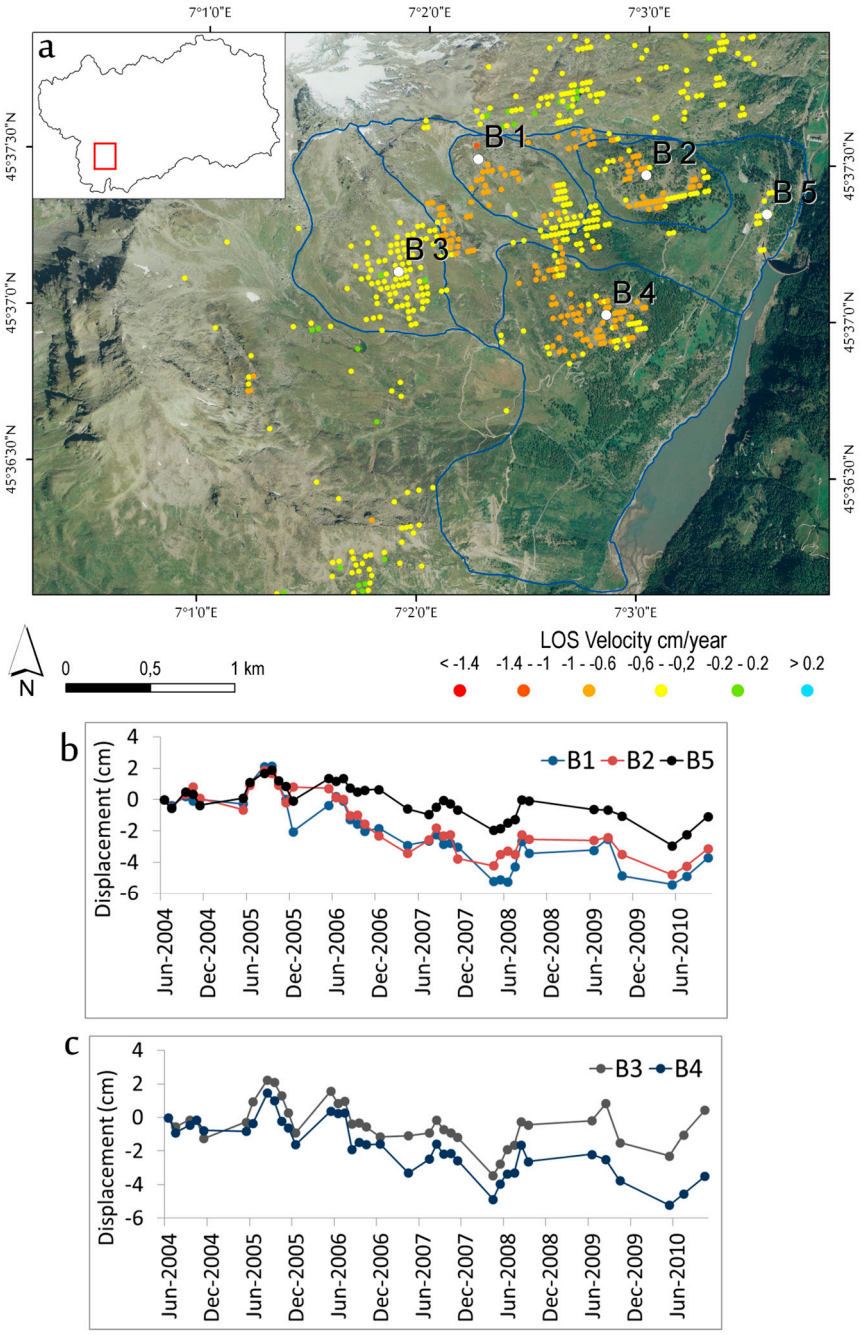


**Figure 8.** (**a**) Mean deformation velocity map of the Beauregard DsGSD case study, for Envisat ascending dataset. (**b**,**c**) Time series corresponding to the targets signed by the **white** dots in the map.

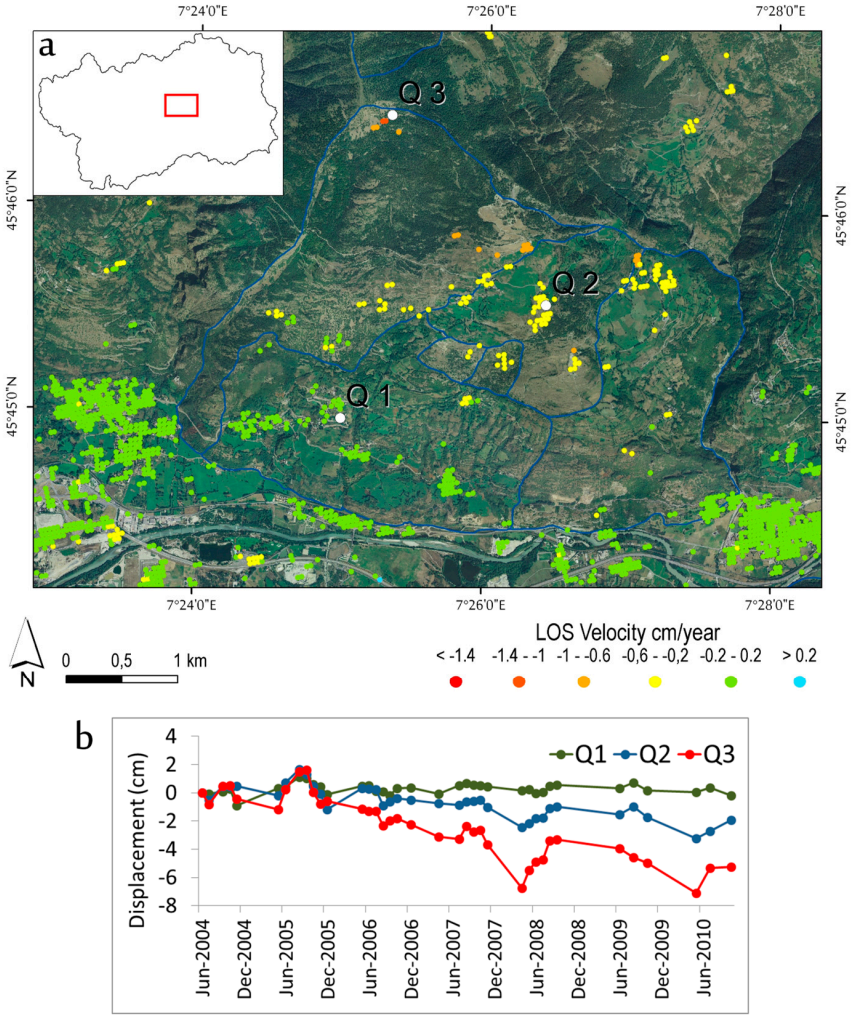


**Figure 9.** (**a**) Mean deformation velocity map of Quart DsGSD case study, for Envisat ascending dataset. (**b**) Time series corresponding to the targets signed by the **white** dots in the map.

In general, we notice a good agreement between our results and the hypothesized kinematic domains presence. In fact, it is possible to identify two distinct portions presenting different LOS velocity values for the observed period: (i) the upper sector, corresponding to the main scarp and constitute by two sub-domains belonging to the DsGSDs (reported in the IFFI project), present velocities ranging from −1.04 up to −0.5 cm/year, while (ii) the basal sector present the lowest LOS velocity, with a range variable from −0.4 to −0.2 cm/year. Moreover, observing Figure 9a, additional kinematic domains can be identified, i.e., a central sector, presenting ground LOS velocities from −0.8 to −0.5 cm/year, and a sector in the west portion of the gravitational phenomenon, characterized by LOS velocities from −0.57 to −0.25 cm/year.

Analyzing the ground deformation time series available for several targets within the phenomenon, we observe a substantially constant deformation rate, represented by a linear trend; however, several accelerations, related to the later spring–summer period, are observed. Specifically, five targets distributed within different Beauregard domains, are presented (Figure 8b,c). The higher displacement of −3.7 cm (away from the satellite), for the observed period from June 2004 and October 2010, was registered by the target B1 located in correspondence to the main scarp of the DsGSD, while the target B5 located in correspondence to the toe of the DsGSD, close to the dam, registered a maximum displacement of −1.07 cm. Instead, a displacement comparable to what was observed for the B1 target, is registered by target B4, with a maximum of −3.5 cm.

The DsGSD of Quart is located on the north side of the broad middle portion of the principal valley. This phenomenon covers an area of about 13 km$^2$ from 530 m a.s.l. at the valley bottom up to 2200 m a.s.l., in the terminal part of the main DsGSD scarp. In [10], the complex evolution of this phenomenon is described, and the ongoing deformation was attributed to an interaction between gravitational movements with glacial and fluvial processes operating over a long time period.

The mean deformation velocity map obtained with GPOD-SBAS processing confirms the ground deformation trend outlined in the literature [10] (Figure 9a) and allows for the identification of ground LOS velocities in the upper and central portions of about −0.8 and −0.6 cm/year, respectively, while lower sectors appear relatively stable over time. Furthermore, in this case, the ground deformation time series generally present a constant deformation rate and show local acceleration during the summer months; the maximum displacement of −5.25 cm for the observed period was registered by the upper sector of the DsGSD (Figure 9b); going down to the valley bottom, the central sector presents a maximum displacement of −1.9 cm, up to −0.2 cm in the lower sector of the slope.

### *4.2. Periglacial Ground Deformations*

We compared the ground velocity map obtained by the GPOD-SBAS and the VDA rock glaciers (RGs) inventory [76]. In general, despite the widespread lack of targets coverage associated with the rock glaciers, we found a fairly good correlation. Considering the ascending orbit, 759 inventoried RGs were observed within the track considered (Table 4); in this case, just the 16% present targets inside, and only 4% present more than ten targets. For the descending orbit, a total of 811 phenomena inventoried are included within the task considered, of which 8% present targets, and only 2% present more than ten targets.

**Table 4.** Summary of the number of rock glaciers, inventoried in the Glacier Inventory, covered by targets generated by the GPOD-SBAS process.

| | Rock Glaciers (from Glaciers Inventory) | Rock Glaciers (within the Track) | Rock Glaciers Covered by Targets | Rock Glaciers with >10 Targets |
|---|---|---|---|---|
| ENVISAT Ascending | 937 | 759 | 123 | 31 |
| ENVISAT Descending | | 811 | 65 | 13 |

The mean deformation velocity maps obtained for both ascending and descending orbits of the Envisat processing results reveal a generally low coverage of the rock glaciers by the targets. Figure 10 shows the mean deformation velocity map detail for the descending orbit acquisition, reporting an example of an intact rock glacier and a relict one. The Petit Emilius (PE in Figure 10a) RG corresponds to the intact one and presents only one target within, with a LOS velocity of −0.8 cm/year, while the Becca di Nona (BN in Figure 10a) RG corresponds to the relict one and presents more than ten targets within, with a mean LOS velocity of −0.5 cm/year, for the entire observed period.

For these two cases, the analysis of the ground deformation time series of the targets (Figure 10b) reveals a constant deformation rate, with a maximum displacement of −1.4 cm for the observed period from September 2004 to October 2010. Analyzing the time series in detail, they seem to display a sort of acceleration in correspondence to the summer and the mid-autumn (e.g., summer 2009). It is worth noting that such phenomena present a seasonal fluctuation [68], where the highest velocities appear during the summer to early autumn months; looking at the results from year to year, comparing the late summer with respect to the early subsequent summer, a moderate acceleration can be observed.

Finally, considering the rock glaciers included within each track (Table 4), we observed in general that the intact rock glaciers present the largest deformation, while, for the rock glaciers identified as relict, a modest displacement, a smaller deformation with respect to the intact ones, was disclosed. In Figure 11, we present the Clapey Gerbioz relict rock glacier example: in ascending orbit (Figure 11a), this RG presents mean LOS velocities from −1.1 cm/year up to −0.26 cm/year; in descending orbit (Figure 11b), a range from −0.7 cm/year up to −0.3 cm/year.

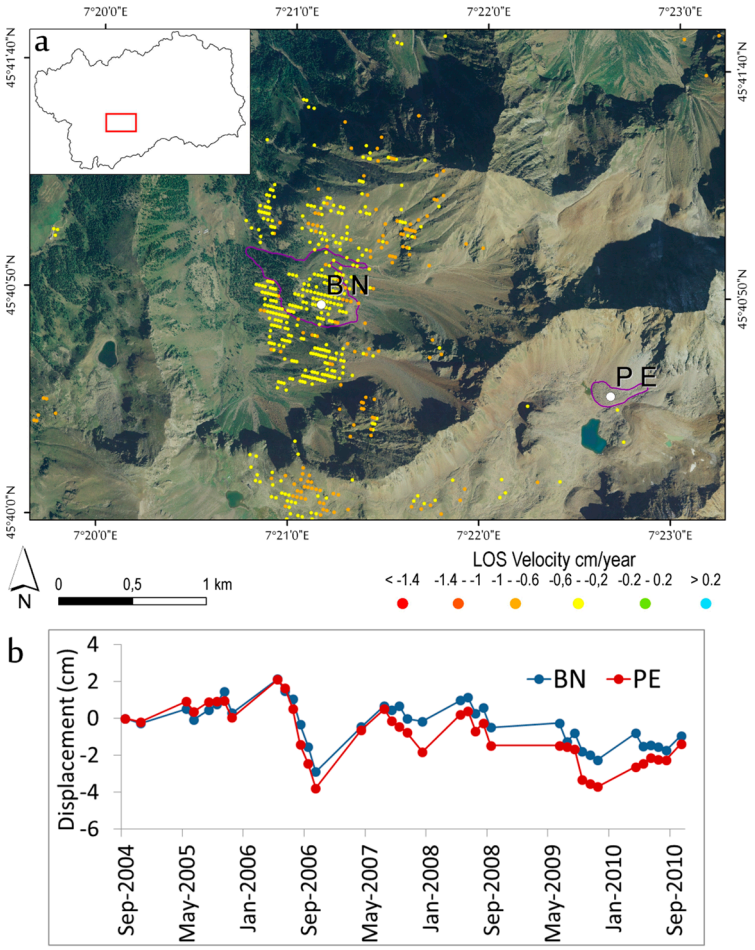


**Figure 10.** (**a**) Mean deformation velocity map of the Becca de Nona (BN) and Petit Emilius (PE) rock glaciers in descending orbit; (**b**) time series corresponding to the targets signed by the **white** dots in the map.

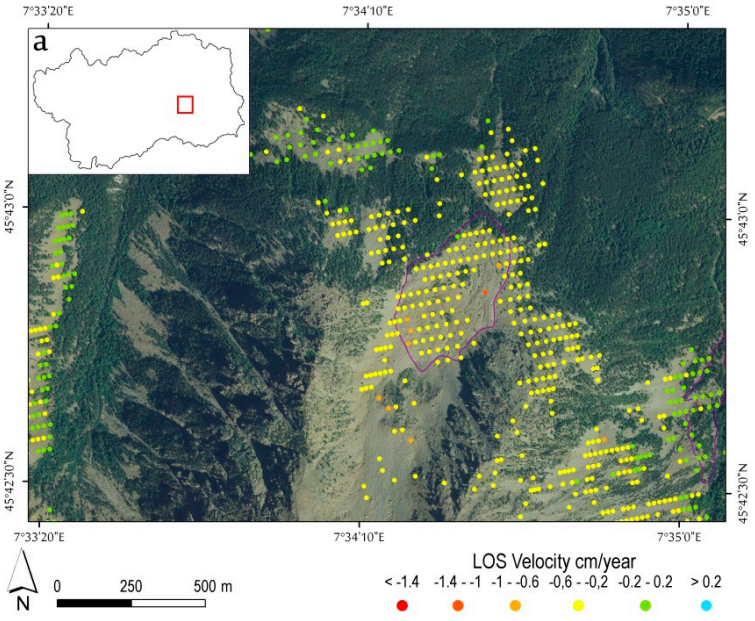


**Figure 11.** *Cont.*

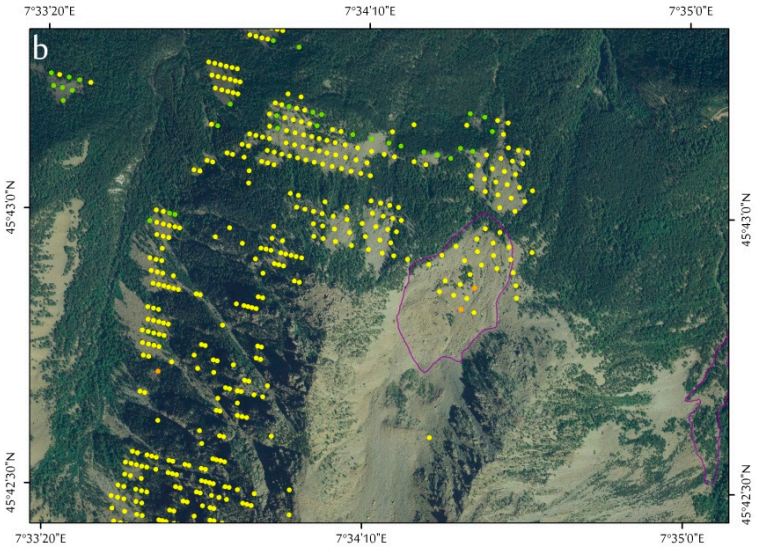


**Figure 11.** Mean deformation velocity map of La Clapey Gerbioz relict rock glacier for (**a**) Envisat ascending orbit and (**b**) descending orbit.

## 5. Discussion

We have shown that the GPOD-SBAS service may allow for the revelation of information about the ground displacements occurring in difficult environments such as high mountain regions.

The GPOD-SBAS service, which is a completely free web-tool, operating on a grid infrastructure, supplies the resources to process an enormous amount of data through the distribution of computing environments via the Parallel-SBAS (P-SBAS) technique [52]. The web-tool operates in an unsupervised manner, processing the P-SBAS chain step-by-step: (i) raw data focusing; (ii) SAR image co-registration: (iii) interferogram generation; (iv) the unwrapping of the computed phases; (v) the generation of the final results. However, in most cases all over the world, the unsupervised manner is not sufficient. For this reason, in order to maximize the number of coherent targets and their distribution over those areas, a number of best practices have to be performed. First, geomorphological and meteo-climatic settings of the study area have to be carefully considered. High topography gradients and complex orography, the predominance of abundant vegetation (e.g., forested areas), and unsuitable valley flank orientation are recognized as challenging environments for DInSAR techniques. The computation of the R-Index [43], considering the satellite's acquisition geometries to analyze the potential distribution of the targets, is important preliminary information. In our example, the prevalent distribution has been observed not only on the south-facing slope in the ERS and Envisat ascending orbits and on the north-facing slope for the descending orbits, for the east–west oriented valleys, but also on the east-facing slope in the ascending orbits and on the west-facing slope in the descending orbits, for the north–south oriented valleys. Moreover, our results have shown the importance of a day-by-day analysis of the meteo-climatic parameters in correspondence to the satellite acquisition epoch, removing the SAR acquisitions affected by snow, causing temporal decorrelation effects. It is worth noting that the crosscheck of the local information obtained by the weather stations parameters available, with the large-scale information provided by the interferograms elaborated by the GPOD-SBAS service, has been crucial. In addition, by fine-tuning the advanced parameters of the GPOD-SBAS service, we have additionally improved the number of coherent targets and their distribution over the study area (Table 2). In particular, we have proved that of the parameter "coherent threshold," which influences the spatial network of the pixels to be unwrapped, mountainous environments have to be increased with respect to the default values, and only very high-quality targets guarantee a significant improvement in the PhU operation. Our study allowed for the obtainment of ground deformation

maps and the associated time series of ERS-1/2 and ASAR-Envisat data, over the entire VDA territory, for the time period respectively from June 1995 to May 2000 and from June 2004 to October 2010.

The comparison of the results obtained for the VDA region to the regional inventory including glaciers, rock glaciers, and DsGSDs shows good general agreement describing the deformation processes of already known phenomena. On glaciers, no displacement has been retrieved due to decorrelation effects caused by their fast evolution. On rock glaciers, a general lack of targets has been observed, limiting the deformation degree establishment (e.g., active, inactive, and relict). In general, an increment in LOS deformation during summer and mid-autumn could be revealed for the intact rock glaciers, while for the relict rock glaciers a slight LOS displacement has been detected, despite the absence of ice within. Finally, on DsGSDs already known and inventoried, a good coverage and distribution of targets have been observed on a regional scale. A downslope velocity deformation comparable with the DsGSDs of very slow moving phenomena [90] has been detected. Moreover, the results obtained showed different activity domains within DsGSD phenomena, in agreement with studies [10,89] of such phenomena in this region, presenting LOS deformation with a linear trend characterized by several acceleration related to the later spring–summer period.

Since in situ measurements suitable for a regional data comparison were not available, we compared our results to the data available on the Portale Cartografico Nazionale [91]. In this web-portal, the ERS-1/2 and ASAR-Envisat acquisitions are processed by the PSInSAR technique, over the entire Italian national territory. For the comparison, we selected a common stable area (Figure 12) and a number of targets presenting significant ground deformation (Figures 13 and 14).

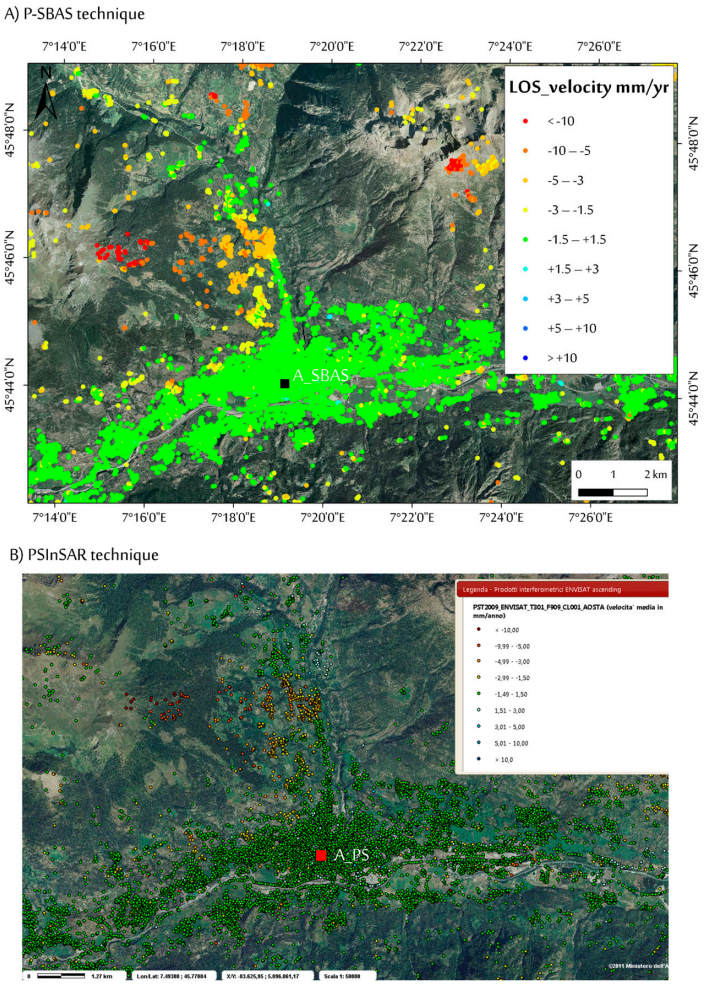


**Figure 12.** *Cont.*

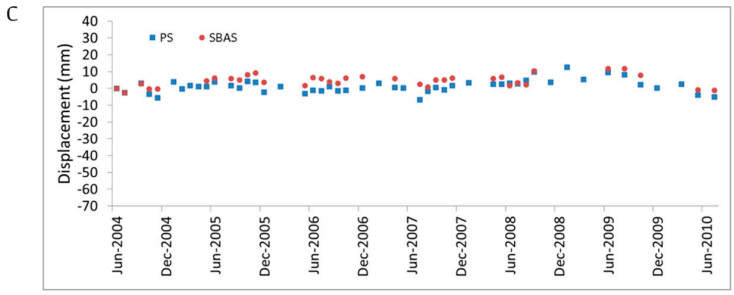


(**a**)

**Figure 12.** Comparison between the Envisat ascending (**A**) GPOD-SBAS results and (**B**) the PSInSAR results (from the Portale Cartografico Nazionale) over the Aosta municipality, considered as common stable area; (**C**) time series corresponding to the SBAS target and the Permanent Scatterers (PS), signified respectively by the **black** square in (**A**) and by the **red** square in (**B**).

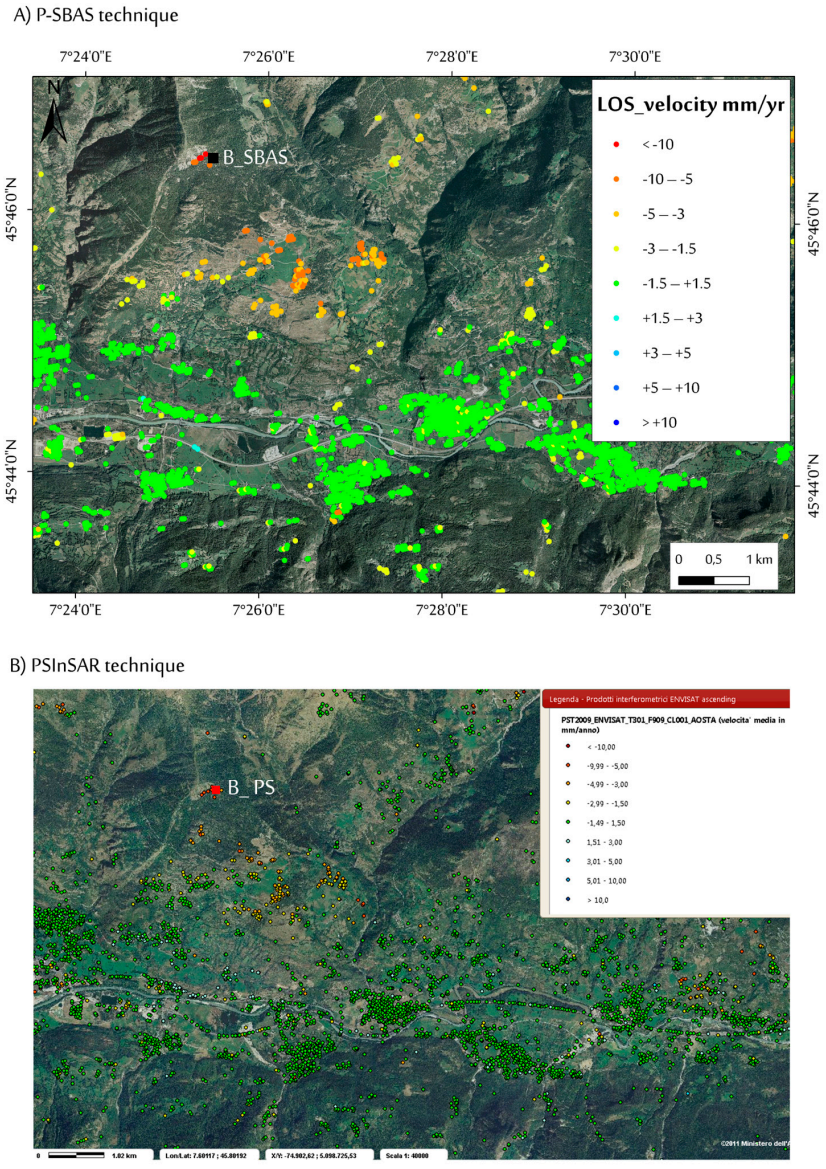


**Figure 13.** *Cont.*

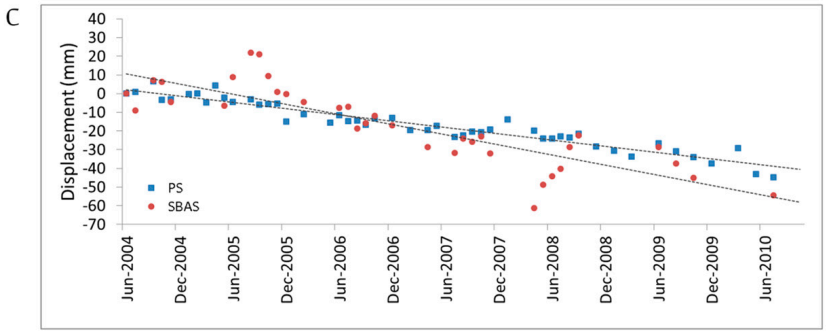


**Figure 13.** Comparison between the Envisat ascending (**A**) GPOD-SBAS results and the (**B**) PSInSAR results (from the Portale Cartografico Nazionale) over the Quart DsGSD; (**C**) time series corresponding to the SBAS target and the PS, signified respectively by the **black** square in (**A**) and by the **red** square in (**B**) within the Quart DsGSD phenomenon.

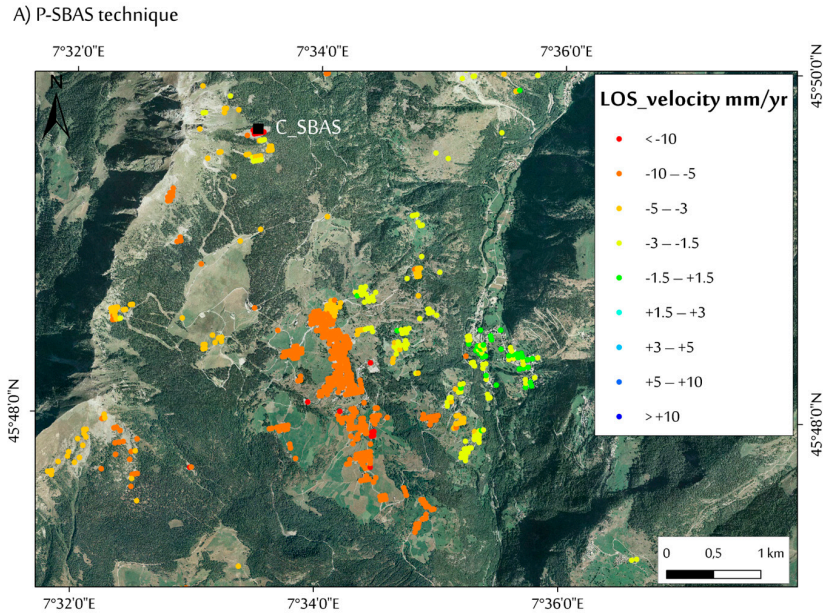


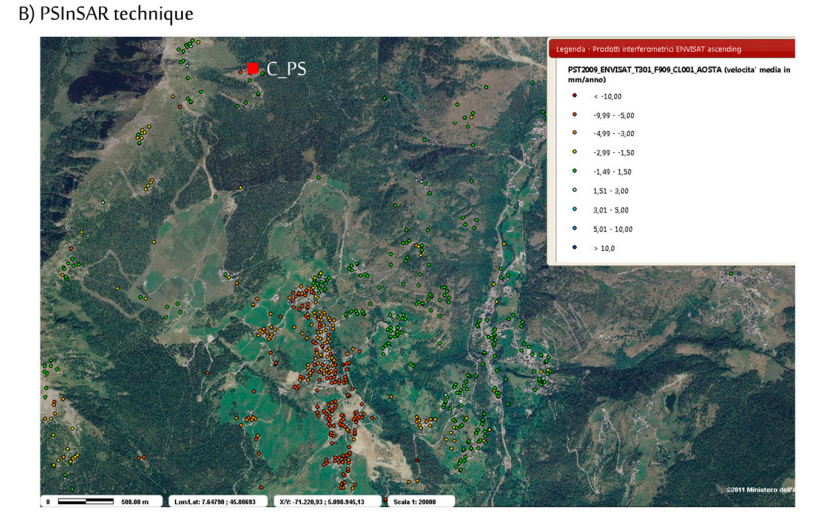


**Figure 14.** *Cont.*

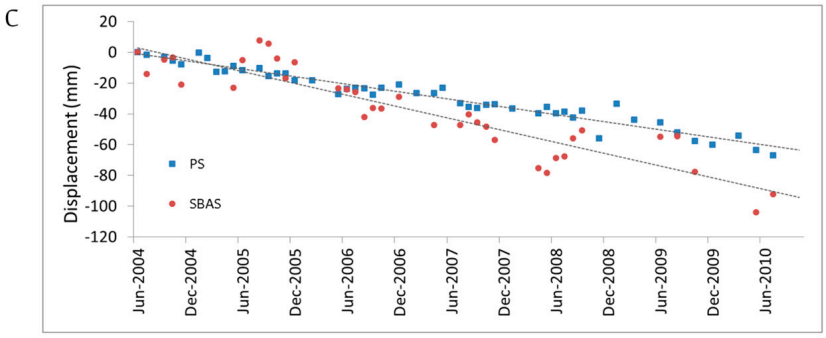


**Figure 14.** Comparison between the Envisat ascending (**A**) GPOD-SBAS results and the (**B**) PSInSAR results (from the Portale Cartografico Nazionale) over the Valtourenenche Valley corresponding to the Mont Meabè rock glacier; (**C**) time series corresponding to the SBAS target and the PS, signified respectively by the **black** square in (**A**) and by the **red** square in (**B**), within the Mont Meabè RG phenomenon.

The comparison shows good agreement between the measurements performed with different DInSAR approaches. Furthermore, the number of SBAS coherent targets and their distribution are comparable with the PS of the Portale Cartografico Nazionale.

## 6. Conclusions

The possibility to investigate surface deformation over wide areas with sub-centimeter accuracy can be very useful for the interpretation of the kinematic behavior of mass wasting phenomena typical of high mountain region (e.g., landslides, rock glaciers, and glaciers). However, the high complex relief, together with the land use and the snow cover, typical of mountainous areas, constitute important limitations for the DInSAR processing applications [42–44,86], also associated to the well-known intrinsic limitations of these techniques [33,45,46].

The proposed iterative procedure, applied through the P-SBAS web-tool within the GPOD environment, allowed us to improve SAR data selection and processing, over high mountain regions. The G-POD user-friendly interface permits to everyone—not just experienced users—quick accessibility to the SAR data and an analysis of SAR data using validated process, without tinkering with the different SBAS-DInSAR processing steps of specific and costly software.

Our processing strategy shows that it is possible to obtain long-term deformation analysis of diverse phenomena affecting mountain areas, and demonstrates how the DInSAR application could obtain reliable information about the ground displacement in the area without in situ instruments. This will be even more evident with the new Sentinel-1 satellite constellation that provides SAR acquisition characterized by significantly reduced revisit time (6 days), which represents an important improvement for the application and exploitation of the DInSAR results.

**Supplementary Materials:** The following are available online at www.mdpi.com/2072-4292/8/10/852/s1; Figure S1: Maps of surface velocities measured along the satellite LOS, for the Envisat dataset in ascending and descending orbit. The four images represent the results of the performed tasks for each orbit using the GPOD-SBAS service.

**Acknowledgments:** The research has been partially supported by HAMMER project, "Relationships between meteo-climatic parameters and ground surface deformation time series in mountain environment," in the framework of the NextData project. The ERS-1/2 and ASAR Envisat data have been provided by ESA. The authors acknowledge Roberto Cuccu of the GPOD support team for providing assistance and help on processing the SAR dataset. The authors are grateful to the four anonymous referees for their comments, which substantially improved the manuscript.

**Author Contributions:** Martina Cignetti processed the dataset by the GPOD-SBAS service, performed the analysis, and wrote the paper. Andrea Manconi and Michele Manunta contributed to process the dataset and supervised the analysis. DanieleGiordan supervised the interpretation of the results from the geomorphological point of view. Claudio De Luca contributed to process the dataset. Francesca Ardizzone has coordinated the work. All authors contributed to paper writing and revision.

**Conflicts of Interest:** The authors declare no conflict of interest.

## References


1. Barsch, D.; Caine, N. The nature of mountain geomorphology. *Mt. Res. Dev.* **1984**, *4*, 287–298. [CrossRef]
2. Kääb, A.; Reynolds, J.M.; Haeberli, W. Glacier and permafrost hazards in high mountains. In *Global Change and Mountain Regions*; Springer: Dordrecht, The Netherlands, 2005; pp. 225–234.
3. Roer, I.; Haeberli, W.; Avian, M.; Kaufmann, V.; Delaloye, R.; Lambiel, C.; Kääb, A. Observations and considerations on destabilizing active rock glaciers in the European Alps. In Proceedings of the Ninth International Conference on Permafrost, Fairbanks, AK, USA, 28 June–3 July 2008.
4. Crozier, M.J. Deciphering the effect of climate change on landslide activity: A review. *Geomorphology* **2010**, *124*, 260–267. [CrossRef]
5. Huggel, C.; Clague, J.J.; Korup, O. Is climate change responsible for changing landslide activity in high mountains? *Earth Surf. Process. Landf.* **2012**, *37*, 77–91. [CrossRef]
6. Augustinus, P. Rock mass strength and the stability of some glacial valley slopes. *Int. J. Rock Mech. Min. Sci. Geomech. Abstr.* **1996**, *33*, 28A–29A.
7. Ballantyne, C.K. Paraglacial geomorphology. *Quat. Sci. Rev.* **2002**, *21*, 1935–2017. [CrossRef]
8. Giardino, M.; Giordan, D.; Ambrogio, S. GIS technologies for data collection, management and visualization of large slope instabilities: Two applications in the Western Italian Alps. *Nat. Hazards Earth Syst. Sci.* **2004**, *4*, 197–211. [CrossRef]
9. Cossart, E.; Braucher, R.; Fort, M.; Bourlès, D.L.; Carcaillet, J. Slope instability in relation to glacial debuttressing in alpine areas (Upper Durance catchment, southeastern France): Evidence from field data and 10Be cosmic ray exposure ages. *Geomorphology* **2008**, *95*, 3–26. [CrossRef]
10. Martinotti, G.; Giordan, D.; Giardino, M.; Ratto, S. Controlling factors for deep-seated gravitational slope deformation (DSGSD) in the Aosta Valley (NW Alps, Italy). *Geol. Soc. Lond. Spec. Publ.* **2011**, *351*, 113–131. [CrossRef]
11. Crosta, G.B.; Frattini, P.; Agliardi, F. Deep seated gravitational slope deformations in the European Alps. *Tectonophysics* **2013**, *605*, 13–33. [CrossRef]
12. Ardizzone, F.; Rossi, M.; Calò, F.; Paglia, L.; Manunta, M.; Mondini, A.C.; Zeni, G.; Reichenbach, P.; Lanari, R.; Guzzetti, F. *Preliminary Analysis of a Correlation between Ground Deformations and Rainfall: The Ivancich Landslide, Central Italy*; SPIE: Bellingham, WA, USA, 2011.
13. Kellerer-Pirklbauer, A.; Kaufmann, V. About the relationship between rock glacier velocity and climate parameters in central Austria. *Austrian J. Earth Sci.* **2012**, *105*, 94–112.
14. Shan, W.; Hu, Z.; Guo, Y.; Zhang, C.; Wang, C.; Jiang, H.; Liu, Y.; Xiao, J. The impact of climate change on landslides in Southeastern of High-Latitude permafrost regions of China. *Front. Earth Sci.* **2015**, *3*. [CrossRef]
15. Fell, R. Landslide risk assessment and acceptable risk. *Can. Geotech. J.* **1994**, *31*, 261–272. [CrossRef]
16. Dai, F.C.; Lee, C.F.; Ngai, Y.Y. Landslide risk assessment and management: An overview. *Eng. Geol.* **2002**, *64*, 65–87. [CrossRef]
17. Fell, R.; Ho Ken, K.S.; Lacasse, S.; Leroi, E. A framework for landslide risk assessment and management. In *Landslide Risk Management*; Taylor & Francis Group: London, UK, 2005; pp. 3–25.
18. Crozier, M.J.; Glade, T. Landslide hazard and risk: Issues, concepts and approach. *Landslide Hazard Risk* **2006**. [CrossRef]
19. Angeli, M.-G.; Pasuto, A.; Silvano, S. A critical review of landslide monitoring experiences. *Eng. Geol.* **2000**, *55*, 133–147. [CrossRef]
20. Corominas, J.; Moya, J.; Lloret, A.; Gili, J.A.; Angeli, M.G.; Pasuto, A.; Silvano, S. Measurement of landslide displacements using a wire extensometer. *Eng. Geol.* **2000**, *55*, 149–166. [CrossRef]
21. Gili, J.A.; Corominas, J.; Rius, J. Using Global Positioning System techniques in landslide monitoring. *Eng. Geol.* **2000**, *55*, 167–192. [CrossRef]
22. Malet, J.-P.; Maquaire, O.; Calais, E. The use of Global Positioning System techniques for the continuous monitoring of landslides: Application to the Super-Sauze earthflow (Alpes-de-Haute-Provence, France). *Geomorphology* **2002**, *43*, 33–54. [CrossRef]
23. Wieczorek, G.F.; Snyder, J.B. Monitoring slope movements. *Geol. Monit.* **2009**. [CrossRef]

24. Giordan, D.; Allasia, P.; Manconi, A.; Baldo, M.; Santangelo, M.; Cardinali, M.; Corazza, A.; Albanese, V.; Lollino, G.; Guzzetti, F. Morphological and kinematic evolution of a large earthflow: The Montaguto landslide, southern Italy. *Geomorphology* **2013**, *187*, 61–79. [CrossRef]
25. Tarchi, D. Monitoring landslide displacements by using ground-based synthetic aperture radar interferometry: Application to the Ruinon landslide in the Italian Alps. *J. Geophys. Res.* **2003**, *108*. [CrossRef]
26. Bitelli, G.; Dubbini, M.; Zanutta, A. Terrestrial laser scanning and digital photogrammetry techniques to monitor landslide bodies. *Int. Arch. Photogramm. Remote Sens. Spat. Inf. Sci.* **2004**, *35*, 246–251.
27. Casagli, N.; Catani, F.; Del Ventisette, C.; Luzi, G. Monitoring, prediction, and early warning using ground-based radar interferometry. *Landslides* **2010**, *7*, 291–301. [CrossRef]
28. Jaboyedoff, M.; Oppikofer, T.; Abellán, A.; Derron, M.-H.; Loye, A.; Metzger, R.; Pedrazzini, A. Use of LIDAR in landslide investigations: A review. *Nat. Hazards* **2012**, *61*, 5–28. [CrossRef]
29. Rosen, P.A.; Hensley, S.; Joughin, I.R.; Li, F.K.; Madsen, S.N.; Rodriguez, E.; Goldstein, R.M. Synthetic aperture radar interferometry. *Proc. IEEE* **2000**, *88*, 333–382. [CrossRef]
30. Nagler, T.; Rott, H.; Kamelger, A. Analysis of landslides in alpine areas by means of SAR interferometry. In Proceedings of the 2002 IEEE International Geoscience and Remote Sensing Symposium, Toront, ON, Canada, 24–28 June 2002.
31. Strozzi, T.; Farina, P.; Corsini, A.; Ambrosi, C.; Thüring, M.; Zilger, J.; Wiesmann, A.; Wegmüller, U.; Werner, C. Survey and monitoring of landslide displacements by means of L-band satellite SAR interferometry. *Landslides* **2005**, *2*, 193–201. [CrossRef]
32. Herrera, G.; Gutiérrez, F.; García-Davalillo, J.C.; Guerrero, J.; Notti, D.; Galve, J.P.; Fernández-Merodo, J.A.; Cooksley, G. Multi-sensor advanced DInSAR monitoring of very slow landslides: The Tena Valley case study (Central Spanish Pyrenees). *Remote Sens. Environ.* **2013**, *128*, 31–43. [CrossRef]
33. Ferretti, A.; Prati, C.; Rocca, F. Permanent scatterers in SAR interferometry. *IEEE Trans. Geosci. Remote Sens.* **2001**, *39*, 8–20. [CrossRef]
34. Berardino, P.; Fornaro, G.; Lanari, R.; Sansosti, E. A new algorithm for surface deformation monitoring based on small baseline differential SAR interferograms. *IEEE Trans. Geosci. Remote Sens.* **2002**, *40*, 2375–2383. [CrossRef]
35. Hooper, A.; Zebker, H.; Segall, P.; Kampes, B. A new method for measuring deformation on volcanoes and other natural terrains using InSAR persistent scatterers: A new persistent scatterers method. *Geophys. Res. Lett.* **2004**, *31*. [CrossRef]
36. Lanari, R.; Zeni, G.; Manunta, M.; Guarino, S.; Berardino, P.; Sansosti, E. An integrated SAR/GIS approach for investigating urban deformation phenomena: A case study of the city of Naples, Italy. *Int. J. Remote Sens.* **2004**, *25*, 2855–2867. [CrossRef]
37. Lanari, R.; Casu, F.; Manzo, M.; Lundgren, P. Application of the SBAS-DInSAR technique to fault creep: A case study of the Hayward fault, California. *Remote Sens. Environ.* **2007**, *109*, 20–28. [CrossRef]
38. Lanari, R.; Berardino, P.; Bonano, M.; Casu, F.; Manconi, A.; Manunta, M.; Manzo, M.; Pepe, A.; Pepe, S.; Sansosti, E.; et al. Surface displacements associated with the L'Aquila 2009 Mw 6.3 earthquake (central Italy): New evidence from SBAS-DInSAR time series analysis: L'aquila earthquake via sbas-dinsar analysis. *Geophys. Res. Lett.* **2010**, *37*. [CrossRef]
39. Guzzetti, F.; Manunta, M.; Ardizzone, F.; Pepe, A.; Cardinali, M.; Zeni, G.; Reichenbach, P.; Lanari, R. Analysis of ground deformation detected using the SBAS-DInSAR technique in Umbria, Central Italy. *Pure Appl. Geophys.* **2009**, *166*, 1425–1459. [CrossRef]
40. Casu, F.; Manzo, M.; Lanari, R. A quantitative assessment of the SBAS algorithm performance for surface deformation retrieval from DInSAR data. *Remote Sens. Environ.* **2006**, *102*, 195–210. [CrossRef]
41. Colesanti, C.; Wasowski, J. Investigating landslides with space-borne Synthetic Aperture Radar (SAR) interferometry. *Eng. Geol.* **2006**, *88*, 173–199. [CrossRef]
42. Notti, D.; Meisina, C.; Zucca, F. Analysis of PSInSAR$^{TM}$ data for landslide studies from regional to local scale. In Proceedings of the Fringe workshop', Frascati, Italy, 23–27 March 2015.
43. Notti, D.; Herrera, G.; Bianchini, S.; Meisina, C.; García-Davalillo, J.C.; Zucca, F. A methodology for improving landslide PSI data analysis. *Int. J. Remote Sens.* **2014**, *35*, 2186–2214.

44. Cigna, F.; Bianchini, S.; Casagli, N. How to assess landslide activity and intensity with Persistent Scatterer Interferometry (PSI): The PSI-based matrix approach. *Landslides* **2013**, *10*, 267–283. [CrossRef]
45. Rocca, F. 3D motion recovery with multi-angle and/or left right interferometry. In Proceedings of the Third International Workshop on ERS SAR, Frascati, Italy, 1–5 December 2003.
46. Colesanti, C.; Wasowski, J. Satellite SAR interferometry for wide-area slope hazard detection and site-specific monitoring of slow landslides. In Proceedings of the Ninth International Symposium on Landslides, Rio de Janeiro, Brazil, 28 June–2 July 2004.
47. Cascini, L.; Fornaro, G.; Peduto, D. Advanced low- and full-resolution DInSAR map generation for slow-moving landslide analysis at different scales. *Eng. Geol.* **2010**, *112*, 29–42. [CrossRef]
48. Ding, X.; Li, Z.; Zhu, J.; Feng, G.; Long, J. Atmospheric effects on InSAR measurements and their mitigation. *Sensors* **2008**, *8*, 5426–5448. [CrossRef]
49. Meisina, C.; Zucca, F.; Notti, D.; Colombo, A.; Cucchi, A.; Savio, G.; Giannico, C.; Bianchi, M. Geological interpretation of PSInSAR data at regional scale. *Sensors* **2008**, *8*, 7469–7492. [CrossRef]
50. Ahmed, R.; Siqueira, P.; Hensley, S.; Chapman, B.; Bergen, K. A survey of temporal decorrelation from spaceborne L-Band repeat-pass InSAR. *Remote Sens. Environ.* **2011**, *115*, 2887–2896. [CrossRef]
51. GRID Processing on Demand. Available online: https://wiki.services.eoportal.org/tiki-custom_home.php (accessed on 31 May 2016).
52. Casu, F.; Elefante, S.; Imperatore, P.; Zinno, I.; Manunta, M.; De Luca, C.; Lanari, R. SBAS-DInSAR parallel processing for deformation time-series computation. *IEEE J. Sel. Top. Appl. Earth Obs. Remote Sens.* **2014**, *7*, 3285–3296. [CrossRef]
53. De Luca, C.; Cuccu, R.; Elefante, S.; Zinno, I.; Manunta, M.; Casola, V.; Rivolta, G.; Lanari, R.; Casu, F. An on-demand web tool for the unsupervised retrieval of earth's surface deformation from SAR data: The P-SBAS service within the ESA G-POD environment. *Remote Sens.* **2015**, *7*, 15630–15650. [CrossRef]
54. Fondazione Montagna Sicura. Available online: http://www.fondazionemontagnasicura.org/ (accessed on 1 June 2015).
55. Elter, G. *La Zona Pennidica Dell'alta e Media Valle d'Aosta e le Unita Limitrofe*; Memorie Istituto Geologico Università: Padova, Italy, 1960.
56. Elter, G. Carte géologique de la Vallée d'Aoste, scale 1:100.000. Consiglio Nazionale delle Ricerche, Società Elaborazioni Cartografiche: Florence, Italy, 1987.
57. Bistacchi, A.; Dal Piaz, G.; Massironi, M.; Zattin, M.; Balestrieri, M. The Aosta-Ranzola extensional fault system and oligocene–present evolution of the Austroalpine-Penninic wedge in the northwestern Alps. *Int. J. Earth Sci.* **2001**, *90*, 654–667. [CrossRef]
58. Dal Piaz, G.V.; Bistacchi, A.; Massironi, M. Geological outline of the Alps. *Episodes* **2003**, *26*, 175–180.
59. De Giusti, F.; Dal Piaz, G.; Massironi, M.; Schiavo, A. Carta geotettonica della Valle d'Aosta. *Mem. Sci. Geol.* **2003**, *55*, 129–149.
60. Gianotti, F.; Forno, M.G.; Ivy-Ochs, S.; Kubik, P.W. New chronological and stratigraphical data on the Ivrea amphitheatre (Piedmont, NW Italy). *Quat. Int.* **2008**, *190*, 123–135. [CrossRef]
61. Mercalli, L. Atlante climatico della Valle d'Aosta. Regione Autonoma Valle d'Aosta. Available online: http://www.regione.vda.it/protezione_civile/edizioni_protezione_civile/atlante_i.aspx (accessed on 16 October 2016).
62. Ratto, S.; Bonetto, F.; Comoglio, C. The October 2000 flooding in Valle d'Aosta (Italy): Event description and land planning measures for the risk mitigation. *Int. J. River Basin Manag.* **2003**, *1*, 105–116. [CrossRef]
63. Kääb, A.; Huggel, C.; Fischer, L.; Guex, S.; Paul, F.; Roer, I.; Salzmann, N.; Schlaefli, S.; Schmutz, K.; Schneider, D. Others remote sensing of glacier-and permafrost-related hazards in high mountains: An overview. *Nat. Hazards Earth Syst. Sci.* **2005**, *5*, 527–554. [CrossRef]
64. Millar, C.I.; Westfall, R.D. Rock glaciers and related periglacial landforms in the Sierra Nevada, CA, USA; inventory, distribution and climatic relationships. *Quat. Int.* **2008**, *188*, 90–104. [CrossRef]
65. Diolaiuti, G.A.; Bocchiola, D.; Vagliasindi, M.; D'Agata, C.; Smiraglia, C. The 1975–2005 glacier changes in Aosta Valley (Italy) and the relations with climate evolution. *Prog. Phys. Geogr.* **2012**, *36*, 764–785. [CrossRef]
66. Haeberli, W. Modern research perspectives relating to permafrost creep and rock glaciers: A discussion. *Permafr. Periglac. Process.* **2000**, *11*, 290–293. [CrossRef]

67. Fallourd, R.; Harant, O.; Trouvé, E.; Nicolas, J.-M.; Gay, M.; Walpersdorf, A.; Mugnier, J.-L.; Serafini, J.; Rosu, D.; Bombrun, L. Others monitoring temperate glacier displacement by multi-temporal TerraSAR-X images and continuous GPS measurements. *IEEE J. Sel. Top. Appl. Earth Obs. Remote Sens.* **2011**, *4*, 372–386. [CrossRef]
68. Delaloye, R.; Lambiel, C.; Gärtner-Roer, I. Overview of rock glacier kinematics research in the Swiss Alps. *Geogr. Helvetica* **2010**, *65*, 135–145. [CrossRef]
69. Barsch, D.P. Rockglaciers as indicators of discontinuous alpine permafrost. An example from the Swiss Alps perspectives in emergency mapping. In Proceedings of the 3rd International Conference Permafrost, Edmonton, AB, Canada, 10–13 July 1978.
70. Barsch, D. Rockglaciers: Indicators for the Present and Former Geoecology in HIGH Mountain Environments. Springer: Berlin, Germany, 1996.
71. Frauenfelder, R.; Kääb, A. Towards a palaeoclimatic model of rock-glacier formation in the Swiss Alps. *Ann. Glaciol.* **2000**, *31*, 281–286. [CrossRef]
72. Seppi, R.; Carton, A.; Baroni, C. Rock glacier relitti e antica distribuzione del permafrost nel Gruppo Adamello Presanella (Alpi Centrali). *Quat. Ital. J. Quat. Sci.* **2010**, *23*, 137–144.
73. Haeberli, W.; Hallet, B.; Arenson, L.; Elconin, R.; Humlum, O.; Kääb, A.; Kaufmann, V.; Ladanyi, B.; Matsuoka, N.; Springman, S.; et al. Permafrost creep and rock glacier dynamics. *Permafr. Periglac. Process.* **2006**, *17*, 189–214. [CrossRef]
74. Guglielmin, M.; Smiraglia, C. The rock glacier inventory of the Italian Alps. In Proceedings of Permafrost, Seventh International Conference, Yellowknife, Canada, 23–27 June 1998.
75. Morra di, C.U.; Letey, S.; Pogliotti, P.; Curtaz, M.; Cremonese, E. Vagliasindi marco nuovo catasto dei rock glaciers della Valle d'Aosta. In *Le Modificazioni Climatiche ei Rischi Naturali*; Polemio, M., Ed.; CNR-IRPI: Bari, Italy, 2011.
76. Catasto Ghiacciai Valle d'Aosta. Available online: http://catastoghiacciai.regione.vda.it/Ghiacciai/MainGhiacciai.html (accessed on 30 November 2015).
77. The Amateur Poker Association and Tour (APAT); Trigila, A. *Rapporto Sulle Frane in Italia: il Progetto IFFI: Metodologia, Risultati e Rapporti Regionali*; APAT: Roma, Australia, 2007.
78. Trigila, A.; Iadanza, C.; Spizzichino, D. Quality assessment of the Italian landslide inventory using GIS processing. *Landslides* **2010**, *7*, 455–470. [CrossRef]
79. Tibaldi, A.; Rovida, A.; Corazzato, C. A giant deep-seated slope deformation in the Italian Alps studied by paleoseismological and morphometric techniques. *Geomorphology* **2004**, *58*, 27–47. [CrossRef]
80. Agliardi, F.; Crosta, G.B.; Zanchi, A.; Ravazzi, C. Onset and timing of deep-seated gravitational slope deformations in the eastern Alps, Italy. *Geomorphology* **2009**, *103*, 113–129. [CrossRef]
81. Agliardi, F.; Crosta, G.; Zanchi, A. Structural constraints on deep-seated slope deformation kinematics. *Eng. Geol.* **2001**, *59*, 83–102. [CrossRef]
82. Notti, D.; Meisina, C.; Zucca, F.; Colombo, A. *Models to Predict Persistent Scatterers Data Distribution and Their Capacity to Register Movement along the Slope*; Fringe Workshop: Frascati, Italy, 2011; pp. 19–23.
83. Pepe, A.; Sansosti, E.; Berardino, P.; Lanari, R. On the generation of ERS/ENVISAT DInSAR time-series via the SBAS technique. *IEEE Geosci. Remote Sens. Lett.* **2005**, *2*, 265–269. [CrossRef]
84. Regione Autonoma Valle d'Aosta Rendiconto Nivometeorologico. Available online: http://appweb.regione.vda.it/dbweb/bollnivometeo/bollnivometeo.nsf/Rendiconto?OpenForm&L=_i& (accessed on 1 November 2015).
85. Centro Funzionale Regione Autonoma Valle d'Aosta Weather Station VDA. Available online: http://cf.regione.vda.it/il_centro_funzionale.php (accessed on 1 September 2015).
86. Wasowski, J.; Bovenga, F. Investigating landslides and unstable slopes with satellite multi temporal interferometry: Current issues and future perspectives. *Eng. Geol.* **2014**, *174*, 103–138. [CrossRef]
87. Pepe, A.; Lanari, R. On the extension of the minimum cost flow algorithm for phase unwrapping of multitemporal differential SAR interferograms. *IEEE Trans. Geosci. Remote Sens.* **2006**, *44*, 2374–2383. [CrossRef]
88. ISPRA Ambiente IFFI Catalogue. Available online: http://www.isprambiente.gov.it/it/progetti/suolo-e-territorio-1/iffi-inventario-dei-fenomeni-franosi-in-italia (accessed on 1 September 2015).
89. Barla, G.; Antolini, F.; Barla, M.; Mensi, E.; Piovano, G. Monitoring of the Beauregard landslide (Aosta Valley, Italy) using advanced and conventional techniques. *Eng. Geol.* **2010**, *116*, 218–235. [CrossRef]

90. Cruden, D.M.; Varnes, D.J. Landslides Types and Processes. In *Landslides: Investigation and Mitigation*; Turner, A.K., Schuster, R.L., Eds.; Transportation Research Board Special Report 247; National Academy Press: Washington, DC, USA, 1996; pp. 36–75.
91. Portale Cartografico Nazionale. Available online: http://www.pcn.minambiente.it/GN/ (accessed on 16 October 2016).